POLITECNICO DI TORINO
Repository ISTITUZIONALE

An invariances-preserving vector basis neural network for the closure of Reynolds-averaged Navier-Stokes equations by the divergence of the Reynolds stress tensor

*Original*
An invariances-preserving vector basis neural network for the closure of Reynolds-averaged Navier-Stokes equations by the divergence of the Reynolds stress tensor / Berrone, S., Oberto, D.. - In: PHYSICS OF FLUIDS. - ISSN 1070-6631. - ELETTRONICO. - 34:9(2022). [10.1063/5.0104605]

*Availability:*
This version is available at: 11583/2971799 since: 2022-09-29T10:25:15Z

*Publisher:*
American Institute of Physics

*Published*
DOI:10.1063/5.0104605

*Terms of use:*

This article is made available under terms and conditions as specified in the corresponding bibliographic description in the repository

*Publisher copyright*

(Article begins on next page)

08 October 2026

Physics of Fluids

# An invariances-preserving vector basis neural network for the closure of Reynolds-averaged Navier–Stokes equations by the divergence of the Reynolds stress tensor

Cite as: Phys. Fluids **34**, 095136 (2022); https://doi.org/10.1063/5.0104605
Submitted: 20 June 2022 • Accepted: 30 August 2022 • Accepted Manuscript Online: 31 August 2022 • Published Online: 27 September 2022

S. Berrone and D. Oberto

View Online Export Citation CrossMark

ARTICLES YOU MAY BE INTERESTED IN

An interpretable framework of data-driven turbulence modeling using deep neural networks
Physics of Fluids **33**, 055133 (2021); https://doi.org/10.1063/5.0048909

DRLinFluids: An open-source Python platform of coupling deep reinforcement learning and OpenFOAM
Physics of Fluids **34**, 081801 (2022); https://doi.org/10.1063/5.0103113

Effect of Reynolds number and blood viscosity models on the left coronary artery with multiple stenoses
Physics of Fluids **34**, 091903 (2022); https://doi.org/10.1063/5.0099822

Physics of Fluids
Special Topic: Hydrogen Flame and Detonation Physics
Submit Today!

AIP Publishing



© 2022 Author(s).

Physics of Fluids ARTICLE scitation.org/journal/phf

# An invariances-preserving vector basis neural network for the closure of Reynolds-averaged Navier–Stokes equations by the divergence of the Reynolds stress tensor

Cite as: Phys. Fluids **34**, 095136 (2022); doi: 10.1063/5.0104605
Submitted: 20 June 2022 · Accepted: 30 August 2022 ·
Published Online: 27 September 2022

View Online Export Citation CrossMark

S. Berrone and D. Oberto[a]

## AFFILIATIONS

Dipartimento di Scienze Matematiche, Politecnico di Torino, Corso Duca degli Abruzzi 24, 10129 Torino, Italy

[a]Author to whom correspondence should be addressed: davide.oberto@polito.it

## ABSTRACT

In the present paper, a new data-driven model is proposed to close and increase accuracy of Reynolds-averaged Navier–Stokes equations. Among the variety of turbulent quantities, it has been decided to predict the divergence of the Reynolds stress tensor (RST). Recent literature works highlighted the potential of this choice. The key novelty of this work is to obtain the divergence of the Reynolds stress tensor through a neural network (NN) whose architecture and input choice guarantee both Galilean and coordinates-frame rotation. The former derives from the input choice of the NN while the latter from the expansion of the divergence of the RST into a vector basis. This approach has been widely used for data-driven models for the RST anisotropy or the RST discrepancies but surprisingly not for the divergence of the RST. The present paper tries to fill this literature gap. Hence, a constitutive relation of the divergence of the RST from mean quantities is proposed to obtain such expansion. Moreover, once the proposed data-driven approach is trained, there is no need to run any classic turbulence model to close the equations. The well-known tests of flow in a square duct and over periodic hills are used to show advantages of the present method compared to the standard turbulence models.

*Published under an exclusive license by AIP Publishing.* https://doi.org/10.1063/5.0104605

## I. INTRODUCTION

Reynolds-averaged Navier–Stokes (RANS) equations are widely used in engineering for turbulent flow simulations. Their popularity comes from the low computational cost compared to large-eddy simulations (LES) and direct numerical simulation (DNS) approaches. However, RANS predictions may be highly inaccurate for some classes of flows[1] due to the bad description of the effects of the Reynolds stresses on the mean flow.[2] On the other hand, thanks to the remarkable growth of high-performance computing facilities, more and more DNS data coming from simple geometries and moderate Reynolds numbers are becoming available. Some classes of flows with DNS datasets are channel flows,[3,4] pipe and duct flows,[5–8] flows over periodic hills,[9,10] and flows around cylinders.[11–13] As a consequence, in the past years an increasing number of studies took advantage of machine learning techniques to exploit DNS data. The remarkable variety of review articles in recent years on the subject highlights this trend.[14–17] In particular, one active research area is focused on data-driven RANS turbulence models that increase accuracy through DNS (or highly accurate LES) data.

In this framework, data-driven models must satisfy the same invariance properties of the physical system they are modeling. Ling *et al.*[18] proved that invariance to coordinates-frame rotation can be guaranteed by taking for each physical dimension ten rotations of the initial dataset and by including them in an augmented dataset. Even if this approach is conceptually valid, it has the huge drawback that for 3D problems, the dataset would become 1000 bigger than the initial one making this method impracticable both in terms of learning time and of memory storage.

Another approach to guarantee invariance properties has been proposed in the pioneering paper of Ling *et al.*[19] In this work, invariance is automatically satisfied by the architecture of the trained neural network (NN). In particular, the NN outputs were the coefficients of the decomposition of the Reynolds stress tensor (RST) anisotropy into a tensor basis defined in Pope,[20] while the inputs were invariant quantities. The obtained neural network was named tensor basis neural network (TBNN). Since then, various studies have been performed to analyze data-driven approaches for the Reynolds stress tensor


Published under an exclusive license by AIP Publishing

anisotropy. A change to the TBNN was proposed to increase accuracy.[21] A convolutional neural network was used for 1D turbulent flows and its interpretability was discussed.[22] Both the coefficients and the basis of the Reynolds stress tensor anisotropy were inferred.[23] This approach was also applied for wind turbine wakes under neutral conditions.[24] The same rotation-invariance idea was used to train random forests able to predict the discrepancy between the Reynolds stress tensor (RST) obtained by a baseline RANS turbulence model and the DNS one.[25,26]

A recent work[27] showed that predicting the divergence of the Reynolds stress tensor, denoted as Reynolds force vector (RFV), instead of the RST itself can effectively increase the accuracy of data-driven RANS turbulence models. On the one hand, the RFV can be obtained from first order statistics reducing intrinsic statistical errors of DNS data. On the other hand, the RFV directly compares into the RANS equations and it seems natural to directly predict it. This work is grounded on these observations and aims to enforce into the RANS system physical invariance properties by construction without data augmentation. Analogously to Ling *et al.* approach,[19] in this work a constitutive assumption of the RFV from mean fields is derived. This hypothesis is fundamental to derive the inputs of the data-driven model and the vector basis used to expand the RFV. The obtained neural network is called vector basis neural network (VBNN). The proposed approach closes the RANS system without the requirements of additional partial differential equations (PDEs) for turbulent scalar quantities or for the RST discrepancies as in previous works. As a consequence, once the model is satisfactorily trained, it does not require any coupling with a classic turbulence model.

Following Sec. I, the paper is organized into four more sections. In Sec. II, a brief overview on RANS models is given to successively describe the TBNN.[19] In Sec. III, the constitutive dependencies of the divergence of the RST are derived. The properties of the VBNN are consequently discussed. The numerical results are presented and discussed in Sec. IV. Classic benchmark flows in a square duct and over periodic hills are chosen as numerical experiments to analyze the data-driven model for two main reasons: (i) availability of highly reliable DNS data in literature; (ii) despite their geometrical simplicity, they represent a powerful proof-of-concept flows because classic RANS turbulence models fail in the prediction of their velocity fields. Finally, in Sec. V, conclusions are drawn.

## II. TENSOR BASIS NEURAL NETWORK

### A. Reynolds-averaged Navier–Stokes equation and turbulence models

The RANS equations for incompressible flows read

$$\begin{cases} \nabla \cdot \mathbf{u} = 0, \\ \dfrac{\partial \mathbf{u}}{\partial t} + \mathbf{u} \cdot \nabla \mathbf{u} - \nu \Delta \mathbf{u} = -\nabla p - \nabla \cdot \boldsymbol{\tau}, \end{cases} \tag{1}$$

where $\mathbf{u}$ is the averaged velocity field, $\nu$ is the kinematic viscosity of the fluid, $p$ is the averaged pressure field divided by the constant density of the fluid, and $\boldsymbol{\tau}$ is the Reynolds Stress Tensor. The latter is a symmetric tensor that needs to be modeled to close the RANS equations and whose components are associated with the correlations of the turbulent fluctuating components of the velocity field. Hence, the divergence of the RST describes the effects of the turbulence on the averaged fields.

One class of turbulence models, called *linear isotropic models*, is based on the well-known Boussinesq hypothesis. The RST is modeled as follows:

$$\boldsymbol{\tau} = \frac{2}{3} k \mathbf{I} - 2\nu_t \mathbf{S}, \tag{2}$$

where $k = \frac{1}{2}\mathrm{tr}(\boldsymbol{\tau})$ is the *turbulent kinetic energy* (tr denotes the trace operator), $\mathbf{I}$ is the identity tensor, $\nu_t$ is the *turbulent viscosity*, and $\mathbf{S} = \frac{1}{2}[\nabla \mathbf{u} + (\nabla \mathbf{u})^T]$ is the mean strain rate tensor. The quantity $\nu_t$ must be modeled, and the system is usually closed by two PDEs (for example one for the turbulent kinetic energy $k$ and one for its dissipation rate $\varepsilon$ using the relation $\nu_t = C_\mu k^2/\varepsilon$ being $C_\mu$ a model's constant). In literature, many different linear turbulence models are defined depending, for example, on the choice of the variables solved to model $\nu_t$.

The linear isotropic models fail in the description of some physical behaviors. As a consequence, more advanced non-linear models have been proposed in literature.[1,20] These models assume an algebraic representation of $\boldsymbol{\tau}$ more complex than in (2). Indeed, they include dependences on high-order powers of the mean strain rate tensor and the mean rotation rate tensor $\mathbf{W} = \frac{1}{2}[\nabla \mathbf{u} - (\nabla \mathbf{u})^T]$.

Another classical approach to close the RANS system (1) is to solve a PDE for each component of the RST tensor.[28–30] This class of models are called Reynolds stress transport models (RSTM). This procedure does not require any modeling of the RST but, on the other hand, require the modeling of some terms inside the PDEs.

Unfortunately, both non-linear and RSTM turbulence models are more likely to diverge compared to classic linear models and, consequently, the latter are still the main option for many flow cases.[31,32]

### B. Tensor basis neural network

Let $a_{ij} = \tau_{ij}/(2k) - 1/3\,\delta_{ij}$ be the anisotropic Reynolds stresses where $\tau_{ij}$ are the Reynolds stresses and $\delta_{ij}$ is the Kronecker delta. In the following, the tensor $\mathbf{a} = a_{ij}$ will be referred to as the Reynolds stress tensor anisotropy. The tensor $\mathbf{a}$ is dimensionless with vanishing trace by definition.

Let $\mathbf{s} = \frac{1}{2}\frac{k}{\varepsilon}[\nabla \mathbf{u} + (\nabla \mathbf{u})^T]$ and $\mathbf{w} = \frac{1}{2}\frac{k}{\varepsilon}[\nabla \mathbf{u} - (\nabla \mathbf{u})^T]$ be the dimensionless counterparts of the mean strain rate tensor $\mathbf{S}$ and mean rotation rate tensor $\mathbf{W}$, respectively, where $\varepsilon$ is the turbulent kinetic energy dissipation rate.

Some classic algebraic turbulence models for the RST can be rephrased as algebraic models for its anisotropic part in terms of $\mathbf{s}$ and $\mathbf{w}$. For example, the classic linear closure (2) is equivalent to $\mathbf{a} = -\frac{\varepsilon}{k^2}\nu_t \mathbf{s}$.

Pope[20] supposed a more general constitutive relation $\mathbf{a} = \mathbf{a}(\mathbf{s}, \mathbf{w})$. This assumption and representation theorems[33] lead to

$$\mathbf{a} = \sum_{j=1}^{10} c_j(\lambda_1, \ldots, \lambda_6)\mathbf{T}_j, \tag{3}$$

where $\lambda_i$, $i = 1, \ldots, 6$, are invariant scalar quantities that depend on $\mathbf{s}$ and $\mathbf{w}$. They are[20,33]

$$\begin{aligned} \lambda_1 &= \mathrm{tr}(\mathbf{s}^2), \quad \lambda_2 = \mathrm{tr}(\mathbf{s}^3), \quad \lambda_3 = \mathrm{tr}(\mathbf{w}^2), \\ \lambda_4 &= \mathrm{tr}(\mathbf{s}\mathbf{w}^2), \quad \lambda_5 = \mathrm{tr}(\mathbf{s}^2\mathbf{w}^2), \quad \lambda_6 = \mathrm{tr}(\mathbf{s}^2\mathbf{w}^2\mathbf{s}\mathbf{w}). \end{aligned} \tag{4}$$

Furthermore, $\mathbf{T}_j$, $j = 1, \ldots, 10$, are


Published under an exclusive license by AIP Publishing

$$\mathbf{T}_1 = \mathbf{s}, \quad \mathbf{T}_2 = \mathbf{sw} - \mathbf{ws}, \quad \mathbf{T}_3 = \mathbf{s}^2 - \frac{1}{3}\mathrm{tr}(\mathbf{s}^2)\mathbf{I},$$
$$\mathbf{T}_4 = \mathbf{w}^2 - \frac{1}{3}\mathrm{tr}(\mathbf{w}^2)\mathbf{I}, \quad \mathbf{T}_5 = \mathbf{ws}^2 - \mathbf{s}^2\mathbf{w},$$
$$\mathbf{T}_6 = \mathbf{w}^2\mathbf{s} + \mathbf{sw}^2 - \frac{2}{3}\mathrm{tr}(\mathbf{sw}^2)\mathbf{I}, \quad \mathbf{T}_7 = \mathbf{wsw}^2 - \mathbf{w}^2\mathbf{sw}, \tag{5}$$
$$\mathbf{T}_8 = \mathbf{sws}^2 - \mathbf{s}^2\mathbf{ws}, \quad \mathbf{T}_9 = \mathbf{w}^2\mathbf{s}^2 + \mathbf{s}^2\mathbf{w}^2 - \frac{2}{3}\mathrm{tr}(\mathbf{s}^2\mathbf{w}^2)\mathbf{I},$$
$$\mathbf{T}_{10} = \mathbf{ws}^2\mathbf{w}^2 - \mathbf{w}^2\mathbf{s}^2\mathbf{w}.$$

Equation (3) states that the Reynolds stress tensor anisotropy can be expressed as a finite linear combination of the 10 tensor basis elements $\{\mathbf{T}_j\}$ listed above. Moreover, the coefficients involved are functions of the six invariants $\{\lambda_i\}$. Both the tensor basis and the invariants are known *a priori*. The only unknowns are the expressions of the ten coefficients $\{c_j\}$.

The formula (3) has been the starting point for Ling *et al.*[19] to define a Tensor Basis Neural Network able to predict the coefficients using the invariants as inputs. Once the coefficients are obtained, the linear combination is computed to obtain $\mathbf{a}$. This approach has the huge advantage that the coefficients are automatically invariant to coordinates-frame rotations and Galilean transformations. This property arises from the Galilean and coordinates-frame rotation invariance of the inputs $\{\lambda_i\}$ that are fed into the TBNN.

## III. VECTOR BASIS NEURAL NETWORK

This section focuses on the vector basis neural network used in this work to close the RANS system by obtaining the $\nabla \cdot \boldsymbol{\tau}$ term.

### A. Constitutive dependencies

Let us define the dimensionless quantity $\widetilde{\nabla \cdot \boldsymbol{\tau}} = \frac{k^{1/2}}{\varepsilon}\nabla \cdot \boldsymbol{\tau}$. In the present work, we assume the constitutive hypothesis,

$$\widetilde{\nabla \cdot \boldsymbol{\tau}} = \mathbf{f}(\mathbf{s}, \mathbf{w}, \widetilde{\nabla \cdot \mathbf{S}}, \widetilde{\nabla k}, Re_d), \tag{6}$$

where $\mathbf{s} = \frac{k}{\varepsilon}\mathbf{S}$, $\mathbf{w} = \frac{k}{\varepsilon}\mathbf{W}$, $\widetilde{\nabla \cdot \mathbf{S}} = \frac{k^{5/2}}{\varepsilon^2}\nabla \cdot \mathbf{S}$, and $\widetilde{\nabla k} = \frac{k^{1/2}}{\varepsilon}\nabla k$ are the dimensionless counterparts of the symmetric part of the velocity gradient $\mathbf{S}$, the antisymmetric part of the velocity gradient $\mathbf{W}$, the divergence of $\mathbf{S}$ and the gradient of $k$, respectively. Finally, $Re_d = \min\left(\frac{\sqrt{k}d}{50\nu}, 2\right)$ is the wall-distance-based Reynolds number, where $d$ is the wall distance. This quantity is relevant during the training process as reported in literature.[25,34] The motivations behind this constitutive choice are discussed in the Appendixes.

With the above hypothesis, following the idea in Ling *et al.*,[19] $\widetilde{\nabla \cdot \boldsymbol{\tau}}$ can be written in a basis made by $N_c = 12$ vectors $\{\mathbf{t}_k\}_{k=1}^{N_c}$ with corresponding coefficients that depend on $N_i = 26$ invariant scalar quantities $\{\lambda_k\}_{k=1}^{N_i}$. In particular, it reads

$$\widetilde{\nabla \cdot \boldsymbol{\tau}} = \sum_{k=1}^{N_c} c_k(\lambda_1, \ldots, \lambda_{N_i})\,\mathbf{t}_k. \tag{7}$$

The appropriate vector basis and the invariants can be obtained from Zheng[33] (Tables I and II). The vector basis reads

**TABLE I.** Root mean square error (RMSE) of VBNN and Baseline models using $\widetilde{\nabla \cdot \boldsymbol{\tau}}^{\mathrm{DNS}}$ as reference.

| Model | RMSE |
|---|---|
| VBNN | $0.32 \times 10^{-1}$ |
| Baseline | $2.43 \times 10^{-1}$ |

**TABLE II.** Maxima of the secondary motion norm and corresponding amplification factor.

| Model | $\max(\|\|(u_y, u_z)^T\|\|_2)/u_b$ | $\frac{\max(\|\|(u_y, u_z)^T\|\|_2)}{\max(\|\|(u_y^{\mathrm{DNS}}, u_z^{\mathrm{DNS}})^T\|\|_2)}$ |
|---|---|---|
| DNS | $2.04 \times 10^{-2}$ | 1 |
| VBNN | $2.65 \times 10^{-2}$ | 1.30 |
| Baseline | $3.47 \times 10^{-2}$ | 1.70 |

$$\begin{gathered}\mathbf{t}_1 = \widetilde{\nabla \cdot \mathbf{S}}, \quad \mathbf{t}_2 = \mathbf{s}\,\widetilde{\nabla \cdot \mathbf{S}}, \quad \mathbf{t}_3 = \mathbf{s}^2\,\widetilde{\nabla \cdot \mathbf{S}},\\ \mathbf{t}_4 = \mathbf{w}\,\widetilde{\nabla \cdot \mathbf{S}}, \quad \mathbf{t}_5 = \mathbf{w}^2\,\widetilde{\nabla \cdot \mathbf{S}}, \quad \mathbf{t}_6 = (\mathbf{sw} + \mathbf{ws})\,\widetilde{\nabla \cdot \mathbf{S}},\\ \mathbf{t}_7 = \widetilde{\nabla k}, \quad \mathbf{t}_8 = \mathbf{s}\,\widetilde{\nabla k}, \quad \mathbf{t}_9 = \mathbf{s}^2\,\widetilde{\nabla k},\\ \mathbf{t}_{10} = \mathbf{w}\,\widetilde{\nabla k}, \quad \mathbf{t}_{11} = \mathbf{w}^2\,\widetilde{\nabla k}, \quad \mathbf{t}_{12} = (\mathbf{sw} + \mathbf{ws})\,\widetilde{\nabla k}.\end{gathered} \tag{8}$$

The invariants are

$$\begin{gathered}\lambda_1 = (\widetilde{\nabla \cdot \mathbf{S}})^T(\widetilde{\nabla \cdot \mathbf{S}}), \quad \lambda_2 = \mathrm{tr}(\mathbf{s}^2), \quad \lambda_3 = \mathrm{tr}(\mathbf{s}^3),\\ \lambda_4 = \mathrm{tr}(\mathbf{w}^2), \quad \lambda_5 = \mathrm{tr}(\mathbf{sw}^2), \quad \lambda_6 = \mathrm{tr}(\mathbf{s}^2\mathbf{w}^2),\\ \lambda_7 = \mathrm{tr}(\mathbf{s}^2\mathbf{w}^2\mathbf{sw}), \quad \lambda_8 = (\widetilde{\nabla \cdot \mathbf{S}})^T\mathbf{s}(\widetilde{\nabla \cdot \mathbf{S}}),\\ \lambda_9 = (\widetilde{\nabla \cdot \mathbf{S}})^T\mathbf{s}^2(\widetilde{\nabla \cdot \mathbf{S}}), \quad \lambda_{10} = (\widetilde{\nabla \cdot \mathbf{S}})^T\mathbf{w}^2(\widetilde{\nabla \cdot \mathbf{S}}),\\ \lambda_{11} = (\widetilde{\nabla \cdot \mathbf{S}})^T\mathbf{sw}(\widetilde{\nabla \cdot \mathbf{S}}), \quad \lambda_{12} = (\widetilde{\nabla \cdot \mathbf{S}})^T\mathbf{s}^2\mathbf{w}(\widetilde{\nabla \cdot \mathbf{S}}),\\ \lambda_{13} = (\widetilde{\nabla \cdot \mathbf{S}})^T\mathbf{wsw}^2(\widetilde{\nabla \cdot \mathbf{S}}), \quad \lambda_{14} = (\widetilde{\nabla k})^T(\widetilde{\nabla k}),\\ \lambda_{15} = (\widetilde{\nabla k})^T\mathbf{s}(\widetilde{\nabla k}), \quad \lambda_{16} = (\widetilde{\nabla k})^T\mathbf{s}^2(\widetilde{\nabla k}),\\ \lambda_{17} = (\widetilde{\nabla k})^T\mathbf{w}^2(\widetilde{\nabla k}), \quad \lambda_{18} = (\widetilde{\nabla k})^T\,\widetilde{\nabla \cdot \mathbf{S}},\\ \lambda_{19} = (\widetilde{\nabla k})^T\mathbf{sw}(\widetilde{\nabla k}), \quad \lambda_{20} = (\widetilde{\nabla k})^T\mathbf{s}^2\mathbf{w}(\widetilde{\nabla k}),\\ \lambda_{21} = (\widetilde{\nabla k})^T\mathbf{wsw}^2(\widetilde{\nabla k}), \quad \lambda_{22} = (\widetilde{\nabla k})^T\mathbf{sw}(\widetilde{\nabla \cdot \mathbf{S}}),\\ \lambda_{23} = (\widetilde{\nabla k})^T\mathbf{s}^2\mathbf{w}(\widetilde{\nabla \cdot \mathbf{S}}), \quad \lambda_{24} = (\widetilde{\nabla k})^T\mathbf{w}(\widetilde{\nabla \cdot \mathbf{S}}),\\ \lambda_{25} = (\widetilde{\nabla k})^T\mathbf{wsw}^2(\widetilde{\nabla \cdot \mathbf{S}}), \quad \lambda_{26} = (\widetilde{\nabla k})^T(\mathbf{sw} + \mathbf{ws})(\widetilde{\nabla \cdot \mathbf{S}}),\\ \lambda_{27} = Re_d,\end{gathered} \tag{9}$$

where the first 26 invariants derive from the dependencies on $\mathbf{s}, \mathbf{w}, \widetilde{\nabla \cdot \mathbf{S}}, \widetilde{\nabla k}$ while the last one is the scalar quantity added in the dependencies assumption (6). The latter is invariant to the choice of the coordinates-frame. The invariant $\mathrm{tr}(\mathbf{s})$ is neglected because identically zero due to the incompressibility constraint.

In Sec. IV, we will consider also the simplified assumption,

$$\widetilde{\nabla \cdot \boldsymbol{\tau}} = \mathbf{f}(\mathbf{s}, \mathbf{w}, \widetilde{\nabla \cdot \mathbf{S}}, Re_d).$$

In this case, the vector basis is formed by the first six vectors in (8) while the invariants are the first 13 and the last one in (9) (they are the expressions that do not involve $\widetilde{\nabla k}$).


Published under an exclusive license by AIP Publishing

## B. Vector basis neural network

### 1. Inputs and outputs

The vector basis neural network outputs are the coefficients $c_j$, $j = 1, \ldots, N_c$, in (7). The VBNN should be able to reproduce the divergence of the RST using only information coming from RANS simulations. In particular, during the training stage, the quantity $\nabla \cdot \boldsymbol{\tau}$ comes from the DNS while the invariants, the vectors, and the adimensionalization factors come from the RANS. Therefore, during the training the optimization process aims to reduce

$$|| \widetilde{(\nabla \cdot \boldsymbol{\tau})}^{\mathrm{DNS}} - \sum_{k=1}^{N_c} c_k^{\mathrm{NN}}(\lambda_1^{\mathrm{RANS}}, \ldots, \lambda_{N_i}^{\mathrm{RANS}})\, \mathbf{t}_k^{\mathrm{RANS}} ||_2. \qquad (10)$$

Here, the quantities $\lambda_i^{\mathrm{RANS}}$, $i = 1, \ldots, N_i$ and $\mathbf{t}_k^{\mathrm{RANS}}$, $k = 1, \ldots, N_c$ come from RANS simulations whereas the quantities $c_k^{\mathrm{NN}}$, $k = 1, \ldots, N_c$, are the neural network outputs. In Eq. (10), with an abuse of notation, we define $\widetilde{(\nabla \cdot \boldsymbol{\tau})}^{\mathrm{DNS}} = \frac{(k^{1/2})^{\mathrm{RANS}}}{\varepsilon^{\mathrm{RANS}}} \nabla \cdot \boldsymbol{\tau}^{\mathrm{DNS}}$. In some cases, the DNS $\varepsilon$ field is not available. For this reason, the dimensionless VBNN output must be successively dimensionalized using RANS fields.

Recent works[27,35,36] proposed indirect approaches to obtain $(\nabla \cdot \boldsymbol{\tau})^{\mathrm{DNS}}$ aiming to reduce errors associated with the lack of statistical convergence in DNS databases. In this work, $(\nabla \cdot \boldsymbol{\tau})^{\mathrm{DNS}}$ is obtained by interpolation of the available $\boldsymbol{\tau}^{\mathrm{DNS}}$ into the RANS mesh followed by computation of its divergence on the RANS mesh.

### 2. Architecture and hyperparameters

The input and output layers of the VBNN have a number of nodes, that is, constrained by the assumption (6). In particular, the input layer has $N_i$ nodes (as many as the invariants) while the output layer has $N_c$ nodes (as many as the coefficients to be predicted), see Fig. 1. In this work, $N_i$ is smaller compared to other models in literature such as Cruz *et al.*[27] where $N_i = 72$.

After some tests, it has been noticed that increasing the depth to more than six hidden layers or the width to more than 30 nodes per hidden layer did not increase the prediction ability of the network. This behavior was observed also in literature.[34] At the end, eight hidden layers have been defined with 30 nodes each as made by Ling *et al.*[19]

It has been observed that the network is not affected by overfitting issues. Thus, the regularization term associated with the weights norm has been shut down. The Adam optimizer[37] is used with learning rate that decreases during the training stage from $10^{-3}$ to $10^{-5}$ and batch size equal to 50. The exponential linear unit[38] (ELU) function has been chosen as activation function because of the better observed performances.

Due to the intrinsic stochasticity of the optimization process, several training runs with the same hyperparameters have been performed. Among them, the run that minimized the validation error has been identified as the reference one for the specific hyperparameters choice.

## C. Invariance properties

### 1. Galilean invariance

Galilean invariance states that the laws of motion are the same in all frames with constant velocities.[26] All the inputs of the VBNN are Galilean invariant because $k$, $\varepsilon$, $\mathbf{S}$, $\mathbf{W}$, $\nabla \cdot \mathbf{S}$ and $\nabla k$ are all Galilean invariant. Consequently, the outputs of the VBNN, that depends on the inputs, do not change through a Galilean transformation.

### 2. Coordinates-frame rotation invariance

Given a rotation matrix $\mathbf{Q}$, the invariants (9) and the vectors (8) follow the transformation law,[18]

$$\begin{aligned} \lambda_i^{\mathbf{Q}} &= \lambda_i, \quad i = 1, \ldots, N_i, \\ \mathbf{t}_k^{\mathbf{Q}} &= \mathbf{Q}\mathbf{t}_k, \quad k = 1, \ldots, N_c, \end{aligned} \qquad (11)$$

where the superscript $\mathbf{Q}$ denotes the representation of the quantity in the rotated coordinates system.

The VBNN is the coordinates-frame rotation invariant in the sense that all the scalar outputs are coordinates-frame rotation invariant. This property directly derives from the invariance of the scalar inputs, i.e., $\lambda_i^{\mathbf{Q}} = \lambda_i$. It implies that $\widetilde{\nabla \cdot \boldsymbol{\tau}}$ transforms correctly under rotations. Indeed

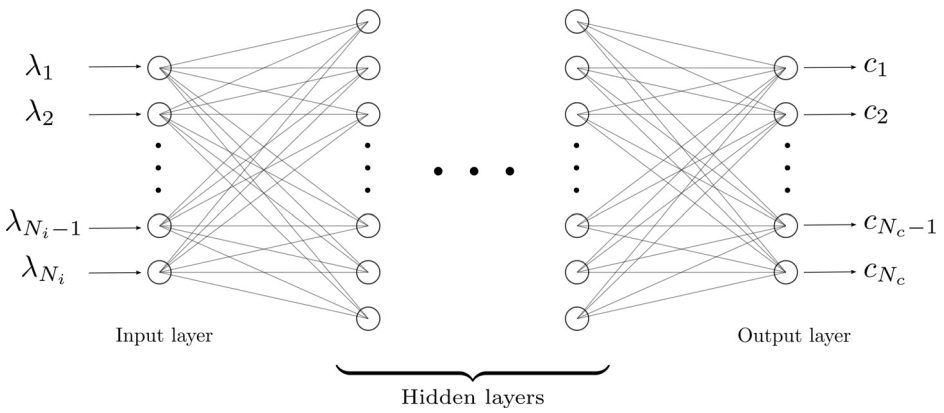


FIG. 1. Architecture of the vector basis neural network.


Published under an exclusive license by AIP Publishing

$$\begin{aligned}\widetilde{\nabla\cdot\boldsymbol{\tau}}^{\mathbf{Q}} &= \sum_{k=1}^{N_c} c_k(\lambda_1^{\mathbf{Q}},\ldots,\lambda_{N_i}^{\mathbf{Q}})\,\mathbf{t}_k^{\mathbf{Q}} \\ &= \sum_{k=1}^{N_c} c_k(\lambda_1,\ldots,\lambda_{N_i})\,\mathbf{Q}\mathbf{t}_k \\ &= \mathbf{Q}\left[\sum_{k=1}^{N_c} c_k(\lambda_1,\ldots,\lambda_{N_i})\,\mathbf{t}_k\right] = \mathbf{Q}\widetilde{\nabla\cdot\boldsymbol{\tau}}. \end{aligned} \tag{12}$$

### D. Implicit–explicit treatment of $\nabla\cdot\boldsymbol{\tau}$

Once the term $\nabla\cdot\boldsymbol{\tau}$ is obtained, the RANS system (1) has to be solved. The easiest approach is to treat explicitly this term like a source term. However, the ill-conditioning of this approach is known[39] when dealing with data-driven Reynolds stress tensor. Consequently, Wu *et al.* proposed to treat implicitly the Reynolds Stress Tensor component aligned to the mean strain rate tensor $\mathbf{S}$ into the diffusive term. A better conditioning of the system was observed with this approach. The present work takes inspiration on this remark with the slight change imposed by dealing with the divergence of the RST instead of the RST itself. Hence, the attention will be devoted to the term aligned with $\nabla\cdot\mathbf{S}$.

Let us take the expression (7) with the first term explicitly written,

$$\widetilde{\nabla\cdot\boldsymbol{\tau}} = c_1\widetilde{\nabla\cdot\mathbf{S}} + \sum_{k=2}^{N_c} c_k\,\mathbf{t}_k. \tag{13}$$

Recalling $\widetilde{\nabla\cdot\boldsymbol{\tau}} = \frac{k^{1/2}}{\varepsilon}\nabla\cdot\boldsymbol{\tau}$ and $\widetilde{\nabla\cdot\mathbf{S}} = \frac{k^{5/2}}{\varepsilon^2}\nabla\cdot\mathbf{S}$, the above expression becomes

$$\nabla\cdot\boldsymbol{\tau} = \frac{k^2}{\varepsilon}\,c_1\nabla\cdot\mathbf{S} + \frac{\varepsilon}{k^{1/2}}\sum_{k=2}^{N_c} c_k\,\mathbf{t}_k. \tag{14}$$

The scalar term $\frac{k^2}{\varepsilon}$ is dimensionally a viscosity. This remark drives to the definition of the *turbulent-like viscosity,*

$$\nu_{tl} := -\frac{k^2}{2\varepsilon}\,c_1. \tag{15}$$

Thus, the momentum equation of the RANS system reads

$$\frac{\partial\mathbf{u}}{\partial t} + \mathbf{u}\cdot\nabla\mathbf{u} - (\nu+\nu_{tl})\Delta\mathbf{u} = -\nabla p - \frac{\varepsilon}{k^{1/2}}\sum_{k=2}^{N_c} c_k\,\mathbf{t}_k. \tag{16}$$

Looking at the obtained system, the difference between the turbulent-like and the turbulent viscosity consists in their positioning with respect to the divergence operator. Indeed, the former is located outside the divergence, i.e., $\nu_{tl}\nabla\cdot(\nabla\mathbf{u})$, while the former inside it, i.e., $\nabla\cdot(\nu_t\nabla\mathbf{u})$, see (1) and (2).

In general, it is not guaranteed that $\nu_{tl} > 0$ (corresponding to $c_1 < 0$) holds everywhere. Let us write $\nu_{tl} = \nu_{tl}^+ + \nu_{tl}^-$ where $\nu_{tl}^+(x) = \max(\nu_{tl}, 0)$ is the positive part of the turbulent-like viscosity. Finally, let us define

$$(\nabla\cdot\boldsymbol{\tau})^\dagger := -\nu_{tl}^-\nabla\cdot\mathbf{S} + \frac{\varepsilon}{k^{1/2}}\sum_{k=2}^{N_c} c_k\,\mathbf{t}_k. \tag{17}$$

The final RANS system with implicit–explicit treatment reads

$$\begin{cases} \nabla\cdot\mathbf{u} = 0, \\ \dfrac{\partial\mathbf{u}}{\partial t} + \mathbf{u}\cdot\nabla\mathbf{u} - (\nu+\nu_{tl}^+)\Delta\mathbf{u} = -\nabla p - (\nabla\cdot\boldsymbol{\tau})^\dagger, \end{cases} \tag{18}$$

where the term associated with $\nu_{tl}^+$ is treated implicitly into the diffusion term while the term $(\nabla\cdot\boldsymbol{\tau})^\dagger$ is treated explicitly.

More details about the implementation of the implicit–explicit treatment in OpenFOAM are given in the Appendixes.

## IV. NUMERICAL RESULTS

This section discusses about the application of the VBNN into two classical benchmark flows: the flow in a square duct and the flow over periodic hills. As it will be discussed, standard RANS models fail in the description of the velocity field in these configurations.

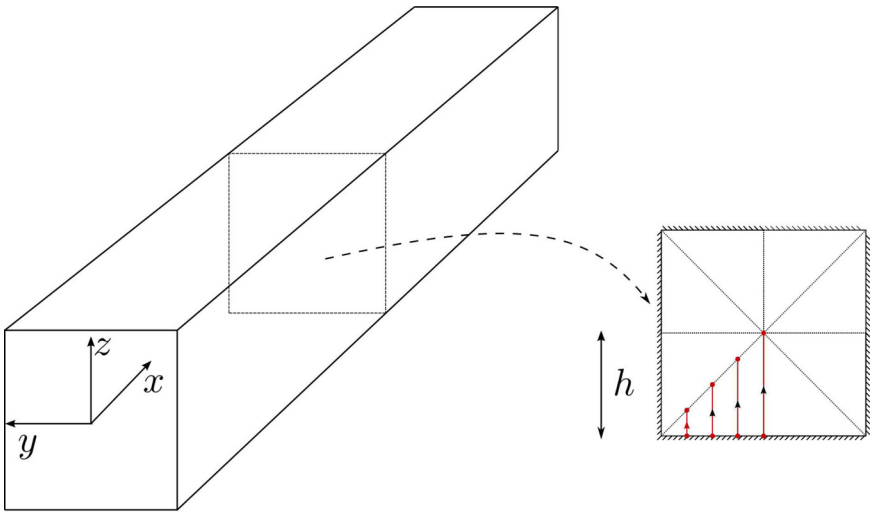


FIG. 2. Square duct domain.


Published under an exclusive license by AIP Publishing

The VBNN is implemented and trained in Python using the Tensorflow package[40] while all the RANS computations are performed with the finite volume method-based OpenFOAM opensource code.[41]

## A. Flow in a square duct

### 1. Dataset

DNS data[6] at several bulk Reynolds numbers $Re_b$ have been used. The simulations with $Re_b = 2200, 2600, 2900$ are employed for training purposes. In particular, 80% of the data are used for training while the remaining 20% for validation. The flow at $Re_b = 3500$ is employed to test the network prediction ability. The test flow Reynolds number is higher than the training ones to analyze the extrapolation property of the VBNN. This particular flow is (in average) stationary and uniform across the main streamwise direction. Only the data coming from three square sections in the central region of the duct are used to reduce considerably the training effort. Figure 2 shows the domain and one square section. The obtained dataset counts roughly $2 \cdot 10^4$ simulation cells. The Launder, Reece, and Rodi (LRR) RSTM[29] is used as RANS model with a low-Reynolds number approach at wall

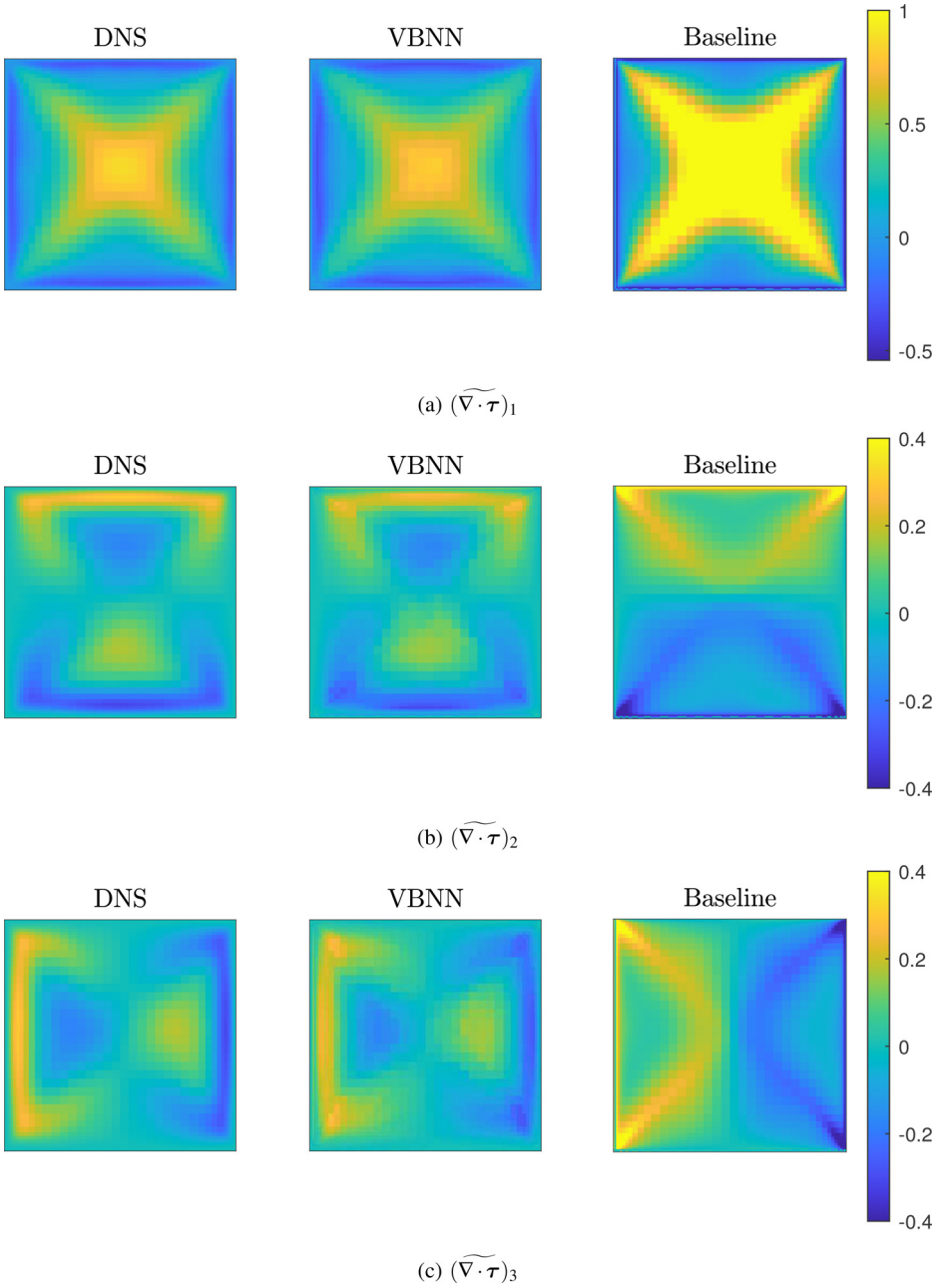


**FIG. 3.** Comparison between first (a), second (b), and third (c) components of $\widetilde{\nabla \cdot \boldsymbol{\tau}}$ from DNS (on the left), VBNN (in the middle) and RSTM Baseline one (on the right).


Published under an exclusive license by AIP Publishing

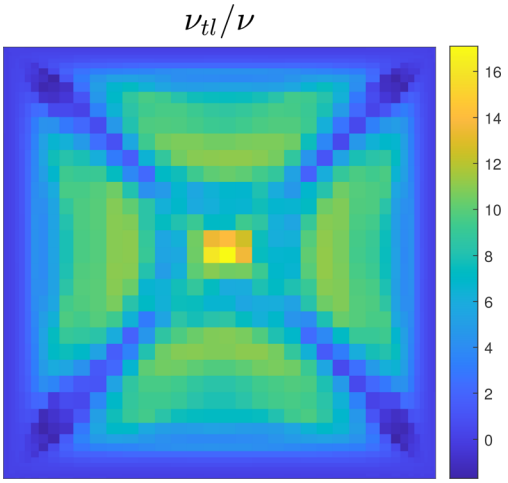


**FIG. 4.** Ratio between turbulent-like viscosity $\nu_{tl}$ and kinematic viscosity $\nu$ in the square section.

(with the first mesh layer thickness such that the maximum value of $y^+$ is around 1). In the following, this turbulence model will be referred to as Baseline.

### 2. Results analysis

Figure 3 compares the components of the vector $\widetilde{\nabla \cdot \boldsymbol{\tau}}$ obtained from DNS, VBNN and Baseline model, respectively. Regarding the first component, the VBNN is in agreement with the DNS both qualitatively and quantitatively while the Baseline overpredicts it in the center and along the diagonals of the square section. Regarding the second and third components, the Baseline have positive and negative values located in two separated square section's halves. In addition, maxima and minima are overestimated in absolute value. On the other hand, the VBNN describes correctly the values of these components and where these are positive and negative. However, VBNN predicts in few cells near the corners maxima or minima that are not in the DNS.

Table I shows the root mean square error (RMSE) defined as follows:

$$\mathrm{RMSE} = \sqrt{\frac{1}{3N_{cells}} \sum_{i=1}^{N_{cells}} ||\widetilde{\nabla \cdot \boldsymbol{\tau}}_i^{\mathrm{DNS}} - \widetilde{\nabla \cdot \boldsymbol{\tau}}_i^{\mathrm{model}}||^2}, \qquad (19)$$

where $N_{cells}$ is the number of cells in the RANS square section grid. This metric quantitatively measures the distance between the DNS dimensionless target and the turbulence model ones. The Baseline RMSE is one order of magnitude higher than the VBNN.

Among all the predicted coefficients in the expansion (7), the first one plays a key role in the conditioning of the RANS system. In particular, the more extended are the regions with a negative predicted first coefficient (and consequently positive $\nu_{tl}$), the better conditioned is the system. Figure 4 shows the ratio between the turbulent-like viscosity $\nu_{tb}$ defined in (15), and the kinematic viscosity $\nu$. The ratio is positive in the majority of the square section with values bigger than eight frequently occurring. The negative regions are very limited and located on the square diagonals near the corners. The minimum value of the ratio is lower than $-1$, in particular $\min(\nu_{tl}/\nu) = -1.70$. If the turbulent-like viscosity was treated completely implicitly, the total viscosity associated with the Laplacian operator in (16) would be negative in some regions. This observation justifies the splitting of $\nu_{tl}$ into its positive and negative part being the former only treated implicitly.

The obtained data-driven $\nabla \cdot \boldsymbol{\tau}$ is successively inserted into the RANS solver to obtain new steady fields. Figure 5 shows the magnitude of the secondary motion $||(u_y, u_z)^T||_2/u_b$ (assuming the streamwise velocity aligned to the $x$ axis), where $u_b$ is the bulk velocity. Lighter colors correspond to higher values of the norm. The different resolution between the models is due to the grid density, being the DNS one much finer than the VBNN and Baseline one (the same grid is employed for both models). Even if the Baseline model describes correctly the regions where the secondary motion is more prominent, it drastically overpredicts it. On the other hand, the VBNN secondary motion is still overpredicted, but its magnitude is in between the DNS case and the Baseline one. To make a quantitative comparison, Table II reports the values of $\max(||(u_y, u_z)^T||_2)/u_b$, and the relative amplification using the DNS value as reference. The VBNN approach reduces the overestimation from 70% of the Baseline model to 30%. Finally, the VBNN secondary motion is characterized by symmetry (up to numerical discrepancies in the central and on the peaks regions) with respect to square section diagonals, while the Baseline case does not correctly respect the symmetry.

Figure 6 shows the velocity components profiles along the red lines defined in Fig. 2 in the lower-left square section quadrant. The $u_y$ has been flipped of sign to make comparison with literature curves[26,39] easier. The Baseline model correctly describes the main motion $u_x$. However, it overpredicts the magnitudes of both secondary motion's velocity components. On the other hand, the VBNN model correctly predicts the secondary motion close to the corners, i.e., for

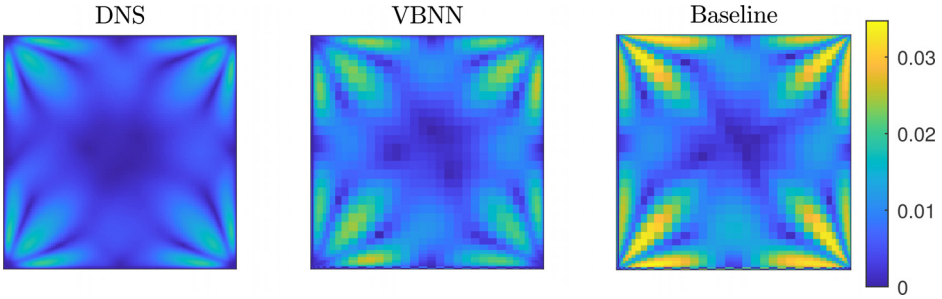


**FIG. 5.** Magnitude of the secondary motion in the DNS (left), the VBNN (middle), and the Baseline model (right). Lighter colors correspond to higher magnitudes of the secondary flow.


Published under an exclusive license by AIP Publishing

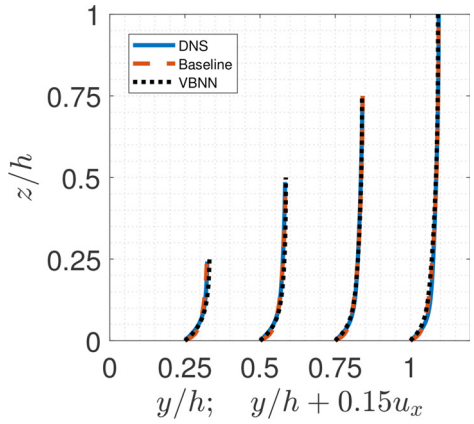


(a)

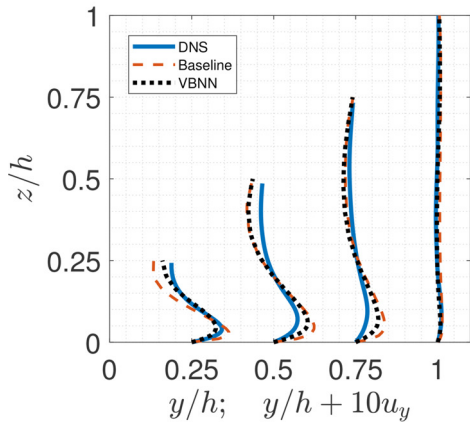


(b)

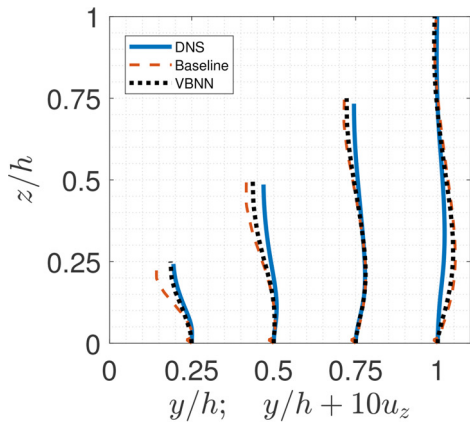


(c)

**FIG. 6.** Primary (a) and secondary motion [(b) and (c)] velocity components along the red lines defined in the square section in Fig. 2. The sign of $u_y$ is changed compared to the coordinates defined in Fig. 2 to make comparison with literature[26,39] easier.

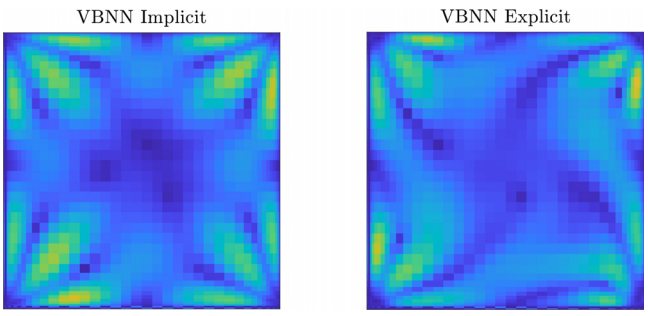


**FIG. 7.** Comparison of the magnitude of the secondary motion in the case of implicit–explicit (left) or purely Explicit (right) treatment of $\nabla \cdot \boldsymbol{\tau}$. The same colormap as in Fig. 5 is used.

$y/h = 0.25$, where the profiles almost overlaps the DNS ones without losing accuracy on the main flow. Small improvements of the secondary motion are also noticeable for the other curves, in particular near wall for $u_y$ curves and far from wall for the $u_z$ ones.

### 3. Role of the implicit–explicit treatment

Figure 7 compares the secondary motion obtained with the implicit–explicit treatment of the divergence of the RST and with the totally explicit one. Even if the latter damps the magnitude of the motion as desired, it unphysically breaks the symmetries. In addition, the explicit simulation takes an order of magnitude more time steps to reach the steady state. In general, a convergence speed-up of implicit treatments is usually observed.[35]

It is important to highlight that differences between the two fields are uniquely due to the treatment of the divergence of the RST into the equations. As a matter of fact, the same $\nabla \cdot \boldsymbol{\tau}$ field is fed into the equations.

### 4. Role of the dependencies choice

In this section, we test also the dependences hypothesis (6) by choosing the simpler relation

$$\widetilde{\nabla \cdot \boldsymbol{\tau}} = \mathbf{f}(\mathbf{s}, \mathbf{w}, \widetilde{\nabla \cdot \mathbf{S}}, Re_d), \tag{20}$$

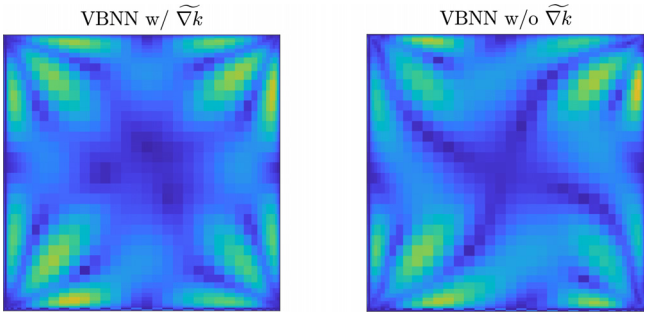


**FIG. 8.** Magnitude of the secondary motion: on the left the field assuming a dependence on $\widetilde{\nabla k}$, on the right the field not assuming a dependence on $\widetilde{\nabla k}$. The same colormap as in Fig. 5 is used.


Published under an exclusive license by AIP Publishing

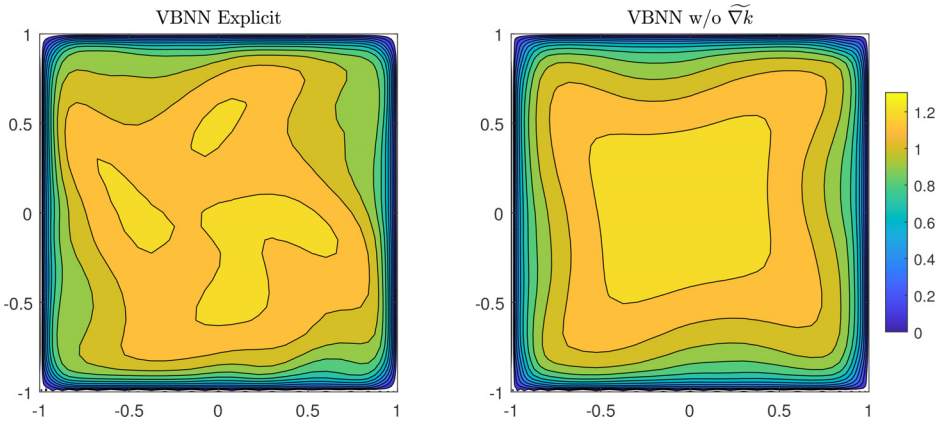


**FIG. 9.** Main motion $u_x/u_b$ with the Explicit treatment and by removing $\widetilde{\nabla k}$ from the dependencies of $\widetilde{\nabla \cdot \boldsymbol{\tau}}$.

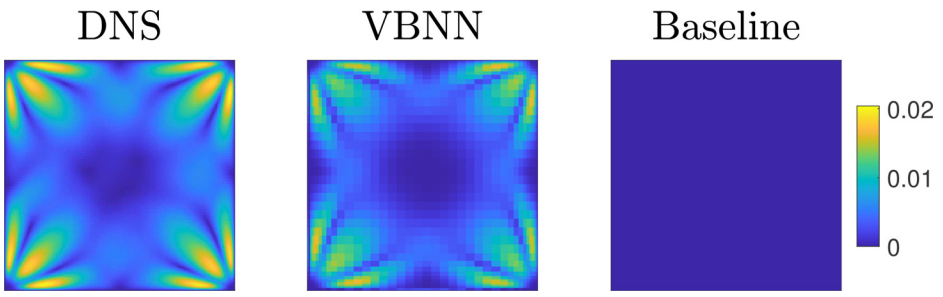


**FIG. 10.** Magnitude of the secondary motion in the DNS (left), the VBNN (middle) and the LS $k-\varepsilon$ Baseline model (right). Lighter colors correspond to higher magnitudes of the secondary flow.

i.e., by removing the dependence on $\widetilde{\nabla k}$. In this case the basis consists of six elements while the invariants are 14. This hypothesis still let possible the implicit–explicit treatment of the RANS system because $\widetilde{\nabla \cdot \mathbf{S}}$ is still a basis vector. This would not be the case if $\widetilde{\nabla \cdot \mathbf{S}}$ were excluded from the dependencies in (6). Considering the results of Sec. IV A 3, the analysis without $\widetilde{\nabla \cdot \mathbf{S}}$ is not carried out.

The RMSE error in this case is $0.37 \times 10^{-1}$, bigger than the corresponding value in Table I. This behavior is expected because a smaller vector basis and a smaller set of invariants are considered.

Figure 8 shows the secondary motion in the two cases. Even when $\widetilde{\nabla k}$ is not considered, the secondary motion is still correctly damped compared to the Baseline case. However, the field loses its symmetry with respect to the square diagonals.

The lack of symmetry of the secondary motion incurred both in the explicit treatment and by removing $\widetilde{\nabla k}$ from the dependencies can compromise the symmetry of the main motion by inducing a non-physical rotation. This phenomenon is confirmed in Fig. 9.

### 5. Role of the Baseline RANS model

Until now, the Launder, Reece, and Rodi RSTM has been used as starting Baseline RANS model to generate the dataset to train the VBNN. While it has been shown that this model overestimates the intensity of the secondary motion, it still predicts this phenomenon. In this section, the Launder and Sharma (LS) $k-\varepsilon$ linear model[42] is used. For the sake of brevity, only the *a posteriori* results concerning the velocity field are shown.

Figure 10 compares the intensity of the secondary motion of the DNS, VBNN and Baseline models. As expected, the Baseline model does not predict secondary motion. On the other hand, the VBNN model predicts it even if underestimated. Analogously to the LRR model case, the intensity of the VBNN model is in between the Baseline and DNS case.

Table III reports the values of $\max(||(u_y, u_z)^T||_2)/u_b$ and the relative attenuation using the DNS value as reference. It confirms the absence of the secondary motion in the Baseline case. The maximum intensity in the VBNN case is 81% the DNS one.

Figure 11 shows the velocity profiles of the primary and secondary flows along the red lines defined in Fig. 2. The $u_x$ profiles of both the Baseline and VBNN models are in agreement with the DNS. As already observed, the Baseline model does not predict any secondary flow while the VBNN predicts non-null $u_y$ and $u_z$ profiles. Regarding $u_y$, the VBNN underestimates the maximum values and slightly

**TABLE III.** Maxima of the secondary motion norm and corresponding amplification factor when using the LS $k-\varepsilon$ as Baseline model.

| Model | $\max(\|\|(u_y, u_z)^T\|\|_2)/u_b$ | $\dfrac{\max(\|\|(u_y, u_z)^T\|\|_2)}{\max(\|\|(u_y^{\mathrm{DNS}}, u_z^{\mathrm{DNS}})^T\|\|_2)}$ |
|---|---|---|
| DNS | $2.04 \times 10^{-2}$ | 1 |
| VBNN | $1.65 \times 10^{-2}$ | 0.81 |
| Baseline | $3.38 \times 10^{-9}$ | $1.66 \times 10^{-7}$ |


Published under an exclusive license by AIP Publishing

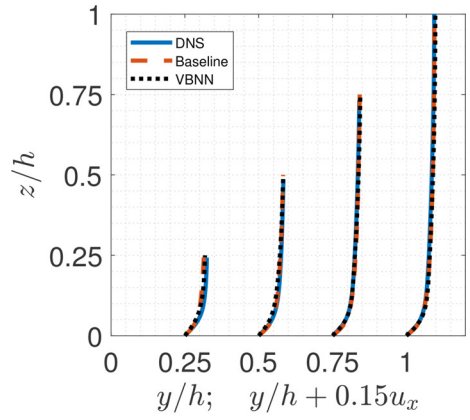


(a)

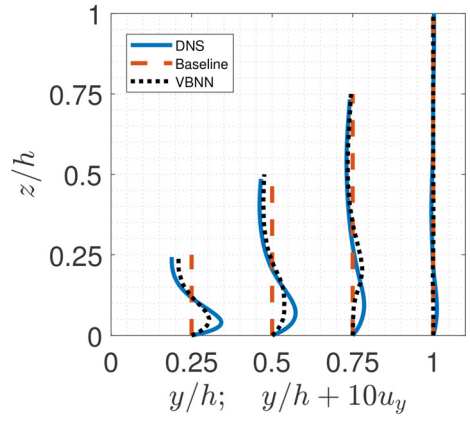


(b)

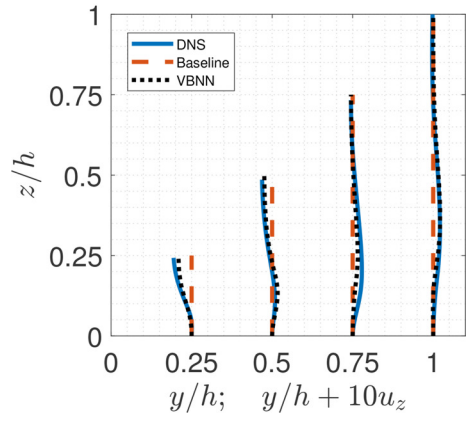


(c)

**FIG. 11.** Primary (a) and secondary motion [(b) and (c)] velocity components along the red lines defined in the square section in Fig. 2. The Baseline model is the LS $k-\varepsilon$ linear model. The sign of $u_y$ is changed compared to the coordinates defined in Fig. 2 to make comparison with literature[26,39] easier.

overestimates the minimum values at $y/h = 0.25$ and $y/h = 0.5$. The maximum at $y/h = 0.75$ is predicted slightly to far from wall. Regarding $u_z$, the VBNN profiles are in agreement with the DNS values.

## B. Flow over periodic hills

### 1. Dataset

The DNS data[10] have been used with different hills geometries but fixed bulk Reynolds number $Re_b = 5600$ are available. Figure 12 shows the different steepness associated with the parameter $\alpha$. The smaller is $\alpha$, the steeper is the hill profile. All lengths are set dimensionless dividing by the hill high $h$.

The flows with $\alpha = 0.5, 0.8, 1.2, 1.5$ have been employed for the training (with the same splitting 80% − 20% for training and validation) while the case with $\alpha = 1.0$ is used for testing only. The RANS simulations have been performed with a 2D domain. The cardinality of the training dataset is about $5.9 \cdot 10^4$ cells, which is the cells number in the 2D RANS domain. It has been observed that a dropout regularization method[43] with drop probability of 0.1 was helpful in the training and consequently adopted. The Launder and Sharma $k-\varepsilon$ linear model is employed as Baseline RANS model. The analysis with the LRR model has not been performed due to convergence issues. All computational details can be found in Xiao *et al.*[10] where the OpenFOAM case is available.

### 2. Results analysis

Figure 13 shows the first two components only of $\widetilde{\nabla \cdot \boldsymbol{\tau}}$ for the DNS, VBNN and Baseline models, being the third component zero (the VBNN correctly predicts it). The VBNN components are in agreement with the reference ones while this is not true for the Baseline model.

For the first component, VBNN provides a correct description of the maxima loci that starts from the crest of the front hill. It also predicts the limited region of local maximum at the middle-end of the first hill and the following minimum. The Baseline case has wrong, both in location and values, maxima and minima in the left part of the domain. It predicts correctly the minima region on the second hill (well predicted by the VBNN model too). However, there is a wrong maximum on the top of the second hill.

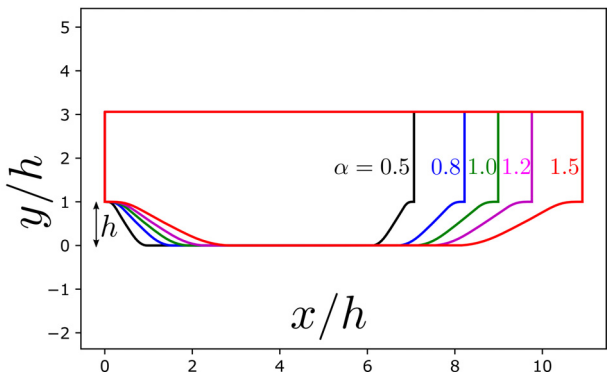


**FIG. 12.** Periodic hills shapes with respect to the $\alpha$ slope parameter.


Published under an exclusive license by AIP Publishing

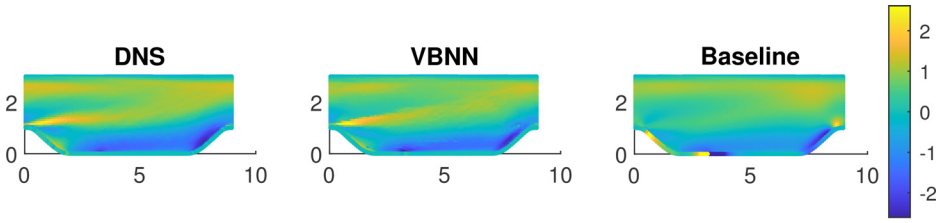


(a) $(\widetilde{\nabla \cdot \boldsymbol{\tau}})_1$

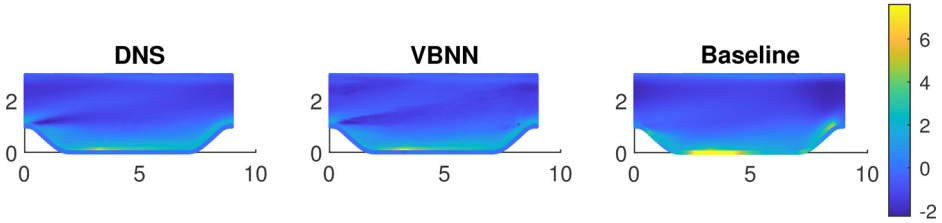


(b) $(\widetilde{\nabla \cdot \boldsymbol{\tau}})_2$

**FIG. 13.** Comparison between first (a) and second (b) components of $\widetilde{\nabla \cdot \boldsymbol{\tau}}$ from the DNS (on the left), the components obtained with the VBNN (in the middle) and the RSTM Baseline one (on the right). The third component is not shown because uniformly zero.

Regarding the second component, the VBNN model describes correctly the value and the extension of the maximum located at $x/h \approx 3.5$, $y/h = 0$, and the Baseline model overpredicts both aspects. Finally, the VBNN case is characterized by the minima region that starts from the first hill crest.

Figure 14 shows $\nu_{tl}/\nu$ to understand the relevance of the implicit–explicit treatment. The ratio is positive in the majority of the domain with the exception of the two region immediately above the hills, predominantly above the rear one. In particular, this quantity assumes values $O(10^2)$ with maximum of about 800. This behavior is helpful for the conditioning of the system. It has been observed that the dropout regularization helps in reducing the regions with negative turbulent-like viscosity.

Figure 15 represents the horizontal velocity profiles along the vertical lines at $x/h = c$ with $c = 0, \ldots, 8$. The profiles are obtained once the simulation reaches the steady state with $\nabla \cdot \boldsymbol{\tau}$ coming from the VBNN model. Figure 15(a) shows the whole domain while Fig. 15(b) focuses on the first hill downstream wall region and Fig. 15(c) depicts the middle top wall region.

Generally speaking, the VBNN curves are closer to the DNS ones compared to the Baseline ones. This behavior is observable in the whole computational domain. It is worth mentioning that the VBNN model predicts, even if underestimated, the local maximum of the horizontal velocity on the crest of the first hill ($x/h = 0$, $y/h = 1$). This behavior is not captured by the Baseline model for which $u_x$ monotonically increases until $y/h \approx 2.8$.

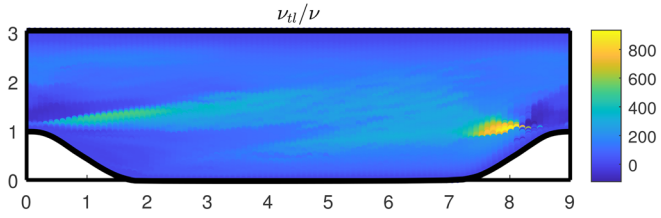


**FIG. 14.** Ratio between turbulent-like viscosity $\nu_{tl}$ and kinematic viscosity $\nu$ in the periodic hills case.

Figure 15(b) shows that the Baseline model predicts almost null reversal flow downstream the first hill and underestimates the size of the recirculation region. These are expected errors when simulating the flow over periodic hills with linear $k - \varepsilon$ models.[44] On the other hand, the VBNN simulation predicts reversal flow quantitatively close to the DNS case for $x/h = 1$ and $x/h = 2$. VBNN still predicts reversal flow, even if underestimated, for $x/h = 3$. However, at $x/h = 4$ the VBNN horizontal velocity is positive near wall while the DNS one is still negative.

Figure 15(c) represents the maxima of the curves that are located near the upper wall ($y/h = 3.036$). The maxima are slightly but constantly underestimated by the Baseline model. Conversely, the VBNN curves are very close to the DNS ones and do not suffer from the underestimation issue.

Figure 16(a) represents the vertical velocity profiles along the vertical lines at $x/h = c$ with $c = 0, \ldots, 8$, while Fig. 16(b) focuses on the

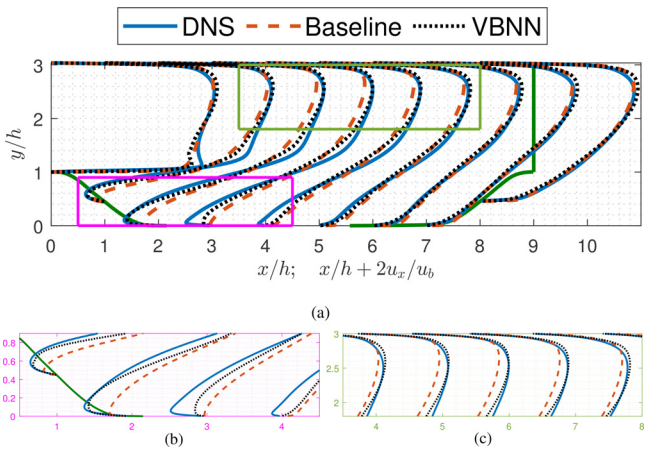


**FIG. 15.** $u_x$ profiles comparison between DNS, VBNN, and Baseline cases (a). Zoom downstream the first hill crest in magenta box in figure above (b). Zoom in the middle top wall region in green box in figure above (c).


Published under an exclusive license by AIP Publishing

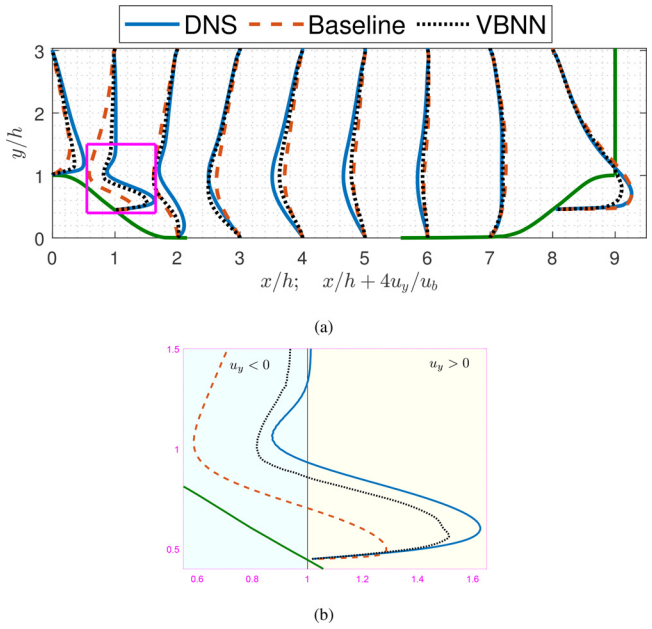


**FIG. 16.** $u_y$ profiles comparison between DNS, VBNN, and Baseline cases (a). Zoom downstream the first hill crest at $x/h = 1$ in magenta box in figure above (b).

$x/h = 1$ line near the hill. VBNN leads to improvements compared to the Baseline $k - \varepsilon$ model, even if less prominent than the $u_x$ case. The region with best improved accuracy is the $x/h = 1$ line near the hill wall represented in Fig. 16(b). The VBNN model predicts a positive velocity region close to the DNS one while the $k - \varepsilon$ turbulence model predicts a positive velocity in a smaller region. In particular, the vertical velocity goes from negative to positive at $y/h \approx 0.93$ in the DNS, $y/h \approx 0.86$ in the VBNN, and $y/h \approx 0.70$ in the $k - \varepsilon$ model.

Finally, it is worth noting that an analysis of the effects of the explicit treatment of $\widetilde{\nabla \cdot \boldsymbol{\tau}}$ on the simulated flow has not been possible due to instability issues.

## V. CONCLUSIONS

The present paper proposes a new data-driven turbulence model to close and increase accuracy of the RANS equations. Hence, the model predicts the divergence of the Reynolds stress tensor, usually called Reynolds force vector.[27] This target vectorial quantity is obtained through a neural network that predicts the coefficients of a vector basis expansion. These coefficients are functions of invariant scalar quantities that depend on the averaged fields. The vector basis and the invariants are uniquely defined once a list of dependencies of the target function is made. A possible dependencies choice is discussed starting from a well-known assumption in literature for the Reynolds stress tensor anisotropy. Moreover, the architecture of the trained network and the invariants choice guarantee both Galilean and coordinates-frame rotation invariances. In addition, this approach closes directly the RANS system and does not require any coupling with classic turbulence models. An implicit treatment of the first term of the expansion is proposed to increase the conditioning of the RANS system.

The proposed model is tested for the flow in a square duct and the flow over periodic hills. Both flows, despite their geometrical simplicity, present features that classic turbulence models do not describe correctly, in particular the secondary flow for the former and the recirculation flow downstream the first hill in the latter. The duct flow case is tested using a classic Launder and Sharma $k - \varepsilon$ linear closure and the Launder, Reece, and Rodi Reynolds stresses transport model. The periodic hills case is tested using the Launder and Sharma $k - \varepsilon$ linear closure. The data-driven model qualitatively and quantitatively outperforms classic turbulence models in both scenarios.

## ACKNOWLEDGMENTS

D. Oberto thanks M. Pintore and F. Della Santa for the valuable advice on the neural networks implementation and A. Giammarini for the discussion on invariance properties. The authors performed this research in the framework of the Italian MIUR Award "Dipartimenti di Eccellenza 2018–2022" granted to the Department of Mathematical Sciences, Politecnico di Torino (CUP: E11G18000350001). S.B. has been supported by the Italian MIUR PRIN Project No. 20204LN5N5_003 and D.O. by the Italian MIUR PRIN Project No. 201752HKH8_003.

## AUTHOR DECLARATIONS

### Conflict of Interest

The authors have no conflicts to disclose.

### Author Contributions

**Stefano Berrone:** Conceptualization (equal); Methodology (equal); Supervision (lead); Writing – original draft (equal). **Davide Oberto:** Conceptualization (equal); Software (lead); Writing – original draft (equal).

## DATA AVAILABILITY

The data that support the findings of this study are available from the corresponding author upon reasonable request.

## APPENDIX A: DEPENDENCIES OF $\widetilde{\nabla \cdot \boldsymbol{\tau}}$

Starting from the definition of RST anisotropy and its expansion in (3), one could write

$$\boldsymbol{\tau} = 2k\left[\sum_{j=1}^{10} c_j(\lambda_1, \ldots, \lambda_6)\,\mathbf{T}_j + \frac{1}{3}\mathbf{I}\right]. \tag{A1}$$

It is possible to compute the divergence of the above expression as follows:

$$\nabla \cdot \boldsymbol{\tau} = \underbrace{2\sum_{j=1}^{10} c_j(\lambda_1, \ldots, \lambda_6)[\nabla k]^T \mathbf{T}_j}_{\alpha} + \underbrace{2\sum_{j=1}^{10} k\left[\nabla c_j(\lambda_1, \ldots, \lambda_6)\right]^T \mathbf{T}_j}_{\beta} + \underbrace{2\sum_{j=1}^{10} k c_j(\lambda_1, \ldots, \lambda_6)\nabla \cdot \mathbf{T}_j}_{\gamma} + \underbrace{\frac{2}{3}\nabla k}_{\delta}. \tag{A2}$$


Published under an exclusive license by AIP Publishing

Let us suppose that both the tensor basis expressed in (5) and the turbulent kinetic energy are known (the standard approach is to obtain them from a RANS simulation). While the terms $\alpha, \gamma, \delta$ can be treated by a neural network that obtains scalar coefficients only, the term $\beta$ contains the gradient of the unknowns that are vector quantities. Thus, the expression (A2) cannot be directly used while preserving coordinates-frame rotation invariance. Nonetheless, it can be used as a guideline to write down a new constitutive law for $\nabla \cdot \boldsymbol{\tau}$ or its dimensionless counterpart $\widetilde{\nabla \cdot \boldsymbol{\tau}} = \frac{k^{1/2}}{\varepsilon} \nabla \cdot \boldsymbol{\tau}$. It has been decided to predict the latter to be as close as possible to the TBNN approach in Ref. 19 where the dimensionless Reynolds Stress Tensor anisotropy is predicted.

From the above computations, it seems natural to suppose dependences of $\widetilde{\nabla \cdot \boldsymbol{\tau}}$ from $\mathbf{s}$, $\mathbf{w}$, their respective divergences and $\nabla k$. It is worth noting that the divergence of each tensors $\{\mathbf{T}_j\}$ in (A2) involves multiplications of $\mathbf{s}$, $\mathbf{w}$ and their respective divergences.

In order to work with dimensionless quantities only, analogously to Ling *et al.*,[19] it has been decided to make the following assumption:

$$\widetilde{\nabla \cdot \boldsymbol{\tau}} = \mathbf{f}(\mathbf{s}, \mathbf{w}, \widetilde{\nabla \cdot \mathbf{S}}, \widetilde{\nabla \cdot \mathbf{W}}, \widetilde{\nabla k}), \tag{A3}$$

where $\mathbf{s} = \frac{k}{\varepsilon}\mathbf{S}$, $\mathbf{w} = \frac{k}{\varepsilon}\mathbf{W}$, $\widetilde{\nabla \cdot \mathbf{S}} = \frac{k^{5/2}}{\varepsilon^2}\nabla \cdot \mathbf{S}$, $\widetilde{\nabla \cdot \mathbf{W}} = \frac{k^{5/2}}{\varepsilon^2}\nabla \cdot \mathbf{W}$, and $\widetilde{\nabla k} = \frac{k^{1/2}}{\varepsilon}\nabla k$ are the dimensionless counterparts of the symmetric part of the velocity gradient $\mathbf{S}$, the antisymmetric part of the velocity gradient $\mathbf{W}$, the divergence of $\mathbf{S}$, the divergence of $\mathbf{W}$, and the gradient of $k$, respectively.

The list of dependences (A3) can be simplified because $\nabla \cdot \mathbf{S} = \nabla \cdot \mathbf{W} = \frac{1}{2}\Delta \mathbf{u}$ from the Schwarz theorem and the incompressibility assumption. Indeed, if $\mathbf{u}$ is sufficiently regular, it holds

$$\nabla \cdot \mathbf{S} = \frac{\partial}{\partial x_j}\frac{1}{2}\left[\frac{\partial u_i}{\partial x_j} + \frac{\partial u_j}{\partial x_i}\right] = \frac{1}{2}\left[\frac{\partial^2 u_i}{\partial x_j^2} + \frac{\partial}{\partial x_i}\frac{\partial u_j}{\partial x_j}\right] = \frac{1}{2}\frac{\partial^2 u_i}{\partial x_j^2},$$
$$\nabla \cdot \mathbf{W} = \frac{\partial}{\partial x_j}\frac{1}{2}\left[\frac{\partial u_i}{\partial x_j} - \frac{\partial u_j}{\partial x_i}\right] = \frac{1}{2}\left[\frac{\partial^2 u_i}{\partial x_j^2} - \frac{\partial}{\partial x_i}\frac{\partial u_j}{\partial x_j}\right] = \frac{1}{2}\frac{\partial^2 u_i}{\partial x_j^2}. \tag{A4}$$

As a consequence, the constitutive assumption can be simplified to

$$\widetilde{\nabla \cdot \boldsymbol{\tau}} = \mathbf{f}(\mathbf{s}, \mathbf{w}, \widetilde{\nabla \cdot \mathbf{S}}, \widetilde{\nabla k}). \tag{A5}$$

In this work, a dependence from $\nabla \cdot \mathbf{S}$ and not from $\nabla \cdot \mathbf{s}$ (both to be made dimensionless) is supposed to make the implicit treatment of the first expansion term straightforwardly.

Finally, as remarked by several authors,[26,34] any other scalar quantity can be included in the constitutive assumption without changing the coordinates-frame rotation property. In particular, in our work we assume an additional dependence from the wall-distance-based Reynolds number $Re_d$.

## APPENDIX B: IMPLICIT–EXPLICIT TREATMENT IN OPENFOAM

The system (18) does not require any coupling with a turbulence model and can theoretically be solved in OpenFOAM with a laminar solver like `icofoam`. The explicit term $(\nabla \cdot \boldsymbol{\tau})^{\dagger}$ is easy to implement because it is sufficient to define a new solver starting from an existing one by adding a fixed source term into the momentum equation.

The implicit term is less trivial to implement. The field $\nu_{tl}^{+}$ cannot be defined as a uniform field as the kinematic viscosity. Therefore, it has been decided to implement a "fake" turbulence model that passes the same $\nu_{tl}^{+}$ field at each solver iteration. Thus, the `simpleFoam` solver is used. To the best knowledge of the authors, OpenFOAM is coded to deal with classic turbulent viscosities that are inside the divergence operator. In order to modify the code as less as possible, it has been decided to solve for an equivalent momentum equation that reads

$$\frac{\partial \mathbf{u}}{\partial t} + \mathbf{u} \cdot \nabla \mathbf{u} - \nabla \cdot \left[(\nu + \nu_{tl}^{+})\nabla \mathbf{u}\right] = -\nabla p - (\nabla \cdot \boldsymbol{\tau})^{\dagger} - \nabla \mathbf{u}\, \nabla \nu_{tl}^{+}. \tag{B1}$$

## REFERENCES


[1] T. Craft, B. Launder, and K. Suga, "Development and application of a cubic eddy-viscosity model of turbulence," Int. J. Heat Fluid Flow **17**, 108–115 (1996).
[2] T. A. Oliver and R. D. Moser, "Bayesian uncertainty quantification applied to RANS turbulence models," J. Phys.: Conf. Ser. **318**, 042032 (2011).
[3] R. D. Moser, J. Kim, and N. N. Mansour, "Direct numerical simulation of turbulent channel flow up to $\mathrm{Re}_\tau = 590$," Phys. Fluids **11**, 943–945 (1999).
[4] H. Abe, H. Kawamura, and Y. Matsuo, "Direct numerical simulation of a fully developed turbulent channel flow with respect to the Reynolds number dependence," J. Fluids Eng. **123**, 382–393 (2001).
[5] S. Pirozzoli, J. Romero, M. Fatica, R. Verzicco, and P. Orlandi, "One-point statistics for turbulent pipe flow up to," J. Fluid Mech. **926**, A28 (2021).
[6] A. Pinelli, M. Uhlmann, A. Sekimoto, and G. Kawahara, "Reynolds number dependence of mean flow structure in square duct turbulence," J. Fluid Mech. **644**, 107–122 (2010).
[7] H. Zhang, F. X. Trias, A. Gorobets, Y. Tan, and A. Oliva, "Direct numerical simulation of a fully developed turbulent square duct flow up to $Re_\tau = 1200$," Int. J. Heat Fluid Flow **54**, 258–267 (2015).
[8] S. Pirozzoli, D. Modesti, P. Orlandi, and F. Grasso, "Turbulence and secondary motions in square duct flow," J. Fluid Mech. **840**, 631–655 (2018).
[9] M. Breuer, N. Peller, C. Rapp, and M. Manhart, "Flow over periodic hills—Numerical and experimental study in a wide range of Reynolds numbers," Comput. Fluids **38**, 433–457 (2009).
[10] H. Xiao, J.-L. Wu, S. Laizet, and L. Duan, "Flows over periodic hills of parameterized geometries: A dataset for data-driven turbulence modeling from direct simulations," Comput. Fluids **200**, 104431 (2020).
[11] F. X. Trias, A. Gorobets, and A. Oliva, "Turbulent flow around a square cylinder at Reynolds number 22,000: A DNS study," Comput. Fluids **123**, 87–98 (2015).
[12] A. Cimarelli, A. Leonforte, and D. Angeli, "Direct numerical simulation of the flow around a rectangular cylinder at a moderately high Reynolds number," J. Wind Eng. Ind. Aerodyn. **174**, 39–49 (2018).
[13] A. Chiarini and M. Quadrio, "The turbulent flow over the BARC rectangular cylinder: A DNS study," Flow Turbul. Combust. **107**, 875–899 (2021).
[14] J. N. Kutz, "Deep learning in fluid dynamics," J. Fluid Mech. **814**, 1–4 (2017).
[15] K. Duraisamy, G. Iaccarino, and H. Xiao, "Turbulence modeling in the age of data," Annu. Rev. Fluid Mech. **51**, 357–377 (2019).
[16] S. L. Brunton, B. R. Noack, and P. Koumoutsakos, "Machine learning for fluid mechanics," Annu. Rev. Fluid Mech. **52**, 477–508 (2020).
[17] R. Vinuesa and S. L. Brunton, "The potential of machine learning to enhance computational fluid dynamics," arXiv:2110.02085 [physics.flu-dyn] (2021).
[18] J. Ling, R. Jones, and J. Templeton, "Machine learning strategies for systems with invariance properties," J. Comput. Phys. **318**, 22–35 (2016).



Published under an exclusive license by AIP Publishing

[19]J. Ling, A. Kurzawski, and J. Templeton, "Reynolds averaged turbulence modelling using deep neural networks with embedded invariance," J. Fluid Mech. **807**, 155–166 (2016).
[20]S. B. Pope, "A more general effective-viscosity hypothesis," J. Fluid Mech. **72**, 331 (1975).
[21]R. Fang, D. Sondak, P. Protopapas, and S. Succi, "Neural network models for the anisotropic Reynolds stress tensor in turbulent channel flow," J. Turbul. **21**, 525–543 (2019).
[22]H. S. de Ocáriz Borde, D. Sondak, and P. Protopapas, "Convolutional neural network models and interpretability for the anisotropic Reynolds stress tensor in turbulent one-dimensional flows," J. Turbul. **23**, 1–28 (2021).
[23]C. Jiang, R. Vinuesa, R. Chen, J. Mi, S. Laima, and H. Li, "An interpretable framework of data-driven turbulence modeling using deep neural networks," Phys. Fluids **33**, 055133 (2021).
[24]J. Steiner, R. P. Dwight, and A. Viré, "Data-driven RANS closures for wind turbine wakes under neutral conditions," Comput. Fluids **233**, 105213 (2022).
[25]J.-X. Wang, J.-L. Wu, and H. Xiao, "Physics-informed machine learning approach for reconstructing Reynolds stress modeling discrepancies based on DNS data," Phys. Rev. Fluids **2**, 034603 (2017).
[26]J.-L. Wu, H. Xiao, and E. Paterson, "Physics-informed machine learning approach for augmenting turbulence models: A comprehensive framework," Phys. Rev. Fluids **3**, 074602 (2018).
[27]M. A. Cruz, R. L. Thompson, L. E. Sampaio, and R. D. Bacchi, "The use of the Reynolds force vector in a physics informed machine learning approach for predictive turbulence modeling," Comput. Fluids **192**, 104258 (2019).
[28]B. E. Launder, G. J. Reece, and W. Rodi, "Progress in the development of a Reynolds-stress turbulence closure," J. Fluid Mech. **68**, 537–566 (1975).
[29]M. M. Gibson and B. E. Launder, "Ground effects on pressure fluctuations in the atmospheric boundary layer," J. Fluid Mech. **86**, 491–511 (1978).
[30]C. G. Speziale, S. Sarkar, and T. B. Gatski, "Modelling the pressure–strain correlation of turbulence: An invariant dynamical systems approach," J. Fluid Mech. **227**, 245–272 (1991).
[31]T. B. Gatski and C. G. Speziale, "On explicit algebraic stress models for complex turbulent flows," J. Fluid Mech. **254**, 59–78 (1993).
[32]B. Basara and S. Jakirlic, "A new hybrid turbulence modelling strategy for industrial CFD," Int. J. Numer. Methods Fluids **42**, 89–116 (2003).
[33]Q.-S. Zheng, "Theory of representations for tensor functions—A unified invariant approach to constitutive equations," Appl. Mech. Rev. **47**, 545–587 (1994).
[34]P. M. Milani, J. Ling, and J. K. Eaton, "Turbulent scalar flux in inclined jets in crossflow: Counter gradient transport and deep learning modelling," J. Fluid Mech. **906**, A27 (2021).
[35]B. P. Brener, M. A. Cruz, R. L. Thompson, and R. P. Anjos, "Conditioning and accurate solutions of Reynolds average Navier–Stokes equations with data-driven turbulence closures," J. Fluid Mech. **915**, A110 (2021).
[36]E. F. Fonseca, V. B. Rangel, B. P. Brener, M. A. Cruz, and R. L. Thompson, "Pre-processing DNS data to improve statistical convergence and accuracy of mean velocity fields in invariant data-driven turbulence models," Theor. Comput. Fluid Dyn. **36**, 435 (2022).
[37]D. P. Kingma and J. Ba, "Adam: A method for stochastic optimization," arXiv:1412.6980 [cs.LG] (2014).
[38]D.-A. Clevert, T. Unterthiner, and S. Hochreiter, "Fast and accurate deep network learning by exponential linear units (ELUS)," arXiv:1511.07289 [cs.LG] (2015).
[39]J. Wu, H. Xiao, R. Sun, and Q. Wang, "Reynolds-averaged Navier–Stokes equations with explicit data-driven Reynolds stress closure can be ill-conditioned," J. Fluid Mech. **869**, 553–586 (2019).
[40]M. Abadi, A. Agarwal, P. Barham, E. Brevdo, Z. Chen, C. Citro, G. S. Corrado, A. Davis, J. Dean, M. Devin, S. Ghemawat, I. Goodfellow, A. Harp, G. Irving, M. Isard, Y. Jia, R. Jozefowicz, L. Kaiser, M. Kudlur, J. Levenberg, D. Mané, R. Monga, S. Moore, D. Murray, C. Olah, M. Schuster, J. Shlens, B. Steiner, I. Sutskever, K. Talwar, P. Tucker, V. Vanhoucke, V. Vasudevan, F. Viégas, O. Vinyals, P. Warden, M. Wattenberg, M. Wicke, Y. Yu, and X. Zheng, "TensorFlow: Large-scale machine learning on heterogeneous systems," arXiv:1603.04467 (2015).
[41]H. G. Weller, G. Tabor, H. Jasak, and C. Fureby, "A tensorial approach to computational continuum mechanics using object-oriented techniques," Comput. Phys. **12**, 620 (1998).
[42]B. Launder and B. Sharma, "Application of the energy-dissipation model of turbulence to the calculation of flow near a spinning disc," Lett. Heat Mass Transfer **1**, 131–137 (1974).
[43]N. Srivastava, G. Hinton, A. Krizhevsky, I. Sutskever, and R. Salakhutdinov, "Dropout: A simple way to prevent neural networks from overfitting," J. Mach. Learn. Res. **15**, 1929–1958 (2014).
[44]C. Rapp, M. Breuer, M. Manhart, and N. Peller, see https://www.kbwiki.ercoftac.org/w/index.php/Abstr:2D_Periodic_Hill_Flow for "UFR 3-30, 2D periodic hill flow."


Published under an exclusive license by AIP Publishing